High-Efficiency Interdigitated Back Contact Silicon Solar Cells with Front Floating Emitter

*Don Ding, Hao Lin, Hong Liu, Guilin Lu, Zhengping Li, Yueheng Zhang, and Wenzhong Shen**

Silicon interdigitated back contact (IBC) solar cells with front floating emitter (FFE-IBC) put forward a new carrier transport concept of "pumping effect" for minority carriers compared with traditional IBC solar cells with front surface field (FSF-IBC). Herein, high-performance FFE-IBC solar cells are achieved theoretically combining superior crystalline silicon quality, front surface passivation, and shallow groove structure using 2D device model. The improvement of minority carrier transport capacity is realized in the conductive FFE layer through optimizing the doping concentration and junction depth. It is shown that the shallow groove on the rear side of FFE-IBC solar cells can effectively enhance the carrier collection ability by means of minimizing the negative impact of undiffused gap or surface p–n junction. The high efficiency exceeding 25% can be realized on silicon FFE-IBC solar cells with the novel cell structure and optimized cell parameters, where the back surface field and emitter region width can be made for the same with only a slight sacrifice of photocurrent density and conversion efficiency. It is demonstrated theoretically that the realization of high-efficiency and low-cost silicon IBC solar cells is feasible due to the increase of the module fabrication tolerance.

1. Introduction

Silicon interdigitated back contact (IBC) solar cell conception was first proposed by Lammert and Schwartz in the 1970s,[1,2] and now is one of the research hotspots of high-efficiency solar cells. The most obvious advantage of IBC solar cells is that metal fingers and busbars are completely removed to the back side. On one hand, the short circuit current can be enhanced due to increased incident photons. On the other

hand, the fill factor can also be improved with decreased contact resistance through optimizing grid line width. Many laboratories and research institutions have achieved satisfactory results in the exploitation of silicon IBC solar cells in recent years, e.g., the efficiency of 23.0% at Fraunhofer institute for solar energy systems (ISE) in Germany (2013),[3] 23.1% at ISFH in Germany (2013),[4] 23.3% at IMEC in Belgium (2013),[5] 24.4% at Trina Solar in China and ANU in Australia (2014),[6] 25.0% at SunPower in USA (2014),[7] and 25.04% at Trina Solar in China (2018).[8] By combining with heterojunction technology, Panasonic in Japan realized heterojunction back contact (HBC) cells of 25.6% efficiency (size 143.7 cm²) in 2014,[9] and Kaneka in Japan has created a world record of 26.3% (2016) and 26.7% (2017) efficiency in the large-area (size 180.4 cm²) HBC silicon solar cells.[10,11] We have recently presented simplified industrial processes to fabricate high-performance silicon IBC solar cells using screen printing and cofiring technologies.[12]

The conventional IBC solar cell, despite its high efficiency, also has electrical shading loss;[13] therefore, the back surface field (BSF) width is generally controlled at about a quarter of the width of the emitter to prevent a large number of carrier recombination over BSF.[14] The inconsistency of BSF and emitter widths results not only in strict patterning tolerances for processing but also has implications for the metallization. Equal widths of both polarities would allow one to metalize the IBC cell with blanket metallization technologies without the need of an isolation layer. This couples with multistep doping technologies and high-temperature processes, making silicon IBC solar cells currently cost about twice as much as the normal silicon solar cells. The Dutch energy research centre of the Netherlands (ECN) put forward a new cell concept "Mercury" by introducing a conductive front floating emitter (FFE) to increase patterning tolerances for interdigitated doping as well as metallization, and using "pumping effect" of FFE for holes generated above the BSF to depress the electrical shading.[15,16] "Pumping effect" utilizes the voltage gradient in FFE layer to enable the holes to transport a longer distance, allowing the BSF width to be as wide as the emitter width without significant loss in cell efficiency. Up to now, ECN and Fraunhofer ISE have achieved the low-cost FFE-IBC solar cells with the

Dr. D. Ding, Dr. H. Lin, Dr. H. Liu, Dr. G. Lu, Dr. Z. Li, Dr. Y. Zhang, Prof. W. Shen
Institute of Solar Energy
Key Laboratory of Artificial Structures and Quantum Control (Ministry of Education)
School of Physics and Astronomy
Shanghai Jiao Tong University
Shanghai 200240, P. R. China
E-mail: wzshen@sjtu.edu.cn

Prof. W. Shen
Collaborative Innovation Center of Advanced Microstructures
Nanjing 210093, P. R. China

The ORCID identification number(s) for the author(s) of this article can be found under https://doi.org/10.1002/pssa.201900445.

DOI: 10.1002/pssa.201900445

top efficiencies of 21.1% and 22.4%, respectively.[17,18] Relevant investigations have also made remarkable progress, for example, the high negative charge density of dielectric Al_2O_3 has better passivation performance for the FFE layer,[19–21] the p–n junction of the overlapping formation of the emitter and BSF diffusion zones leads to more carrier recombination,[18–20] FFE-IBC solar cells show less efficiency loss at low illumination intensity than standard p-type H pattern cells,[15,22] FFE-IBC solar cells have higher conversion efficiency (Eff) than n-type passivated emitter rear totally diffused (n-PERT) cells under the same conditions.[23]

Although the IBC solar cells can yield more photogenerated carriers as a result of the elimination for optical shading loss, the carriers have various losses before being collected by the electrodes,[24,25] such as Shockley–Read–Hall (SRH) loss, Auger recombination, interface recombination, and non-ohm-contact recombination loss. The continuous reduction of carrier recombination losses has always been a subject for scientific research institutions and enterprises.[26,27] We notice that the carrier recombination loss over BSF region can be effectively lessened via lateral hole transport in the FFE layer (i.e., restraining the electrical shading loss), but the recombination loss can also occur when minority carriers transport to the back side of the solar cells (e.g., the recombination caused by undiffused gap or surface p–n junction).[28,29] In this work, we have theoretically proposed ways to improve the Eff of the FFE-IBC solar cells. One significant way is to boost carrier collection probability by means of making undiffused gap and surface p–n junction reduced or disappeared completely with designed shallow grooves construction at the back side. Photoelectric simulation shows that the optimal Eff of the novel FFE-IBC solar cell can be over 25%.

2. Device Structure and Simulation Methods

Figure 1a1, a2 shows the schematic structure of the reference silicon IBC solar cells and the investigated silicon FFE-IBC solar cells with the doped FFE and shallow grooves. The introduction of groove in the interdigitated distribution of emitter and BSF can make the emitter doping and BSF doping located in the different positions from the rear surface, and avoid the repeated usage for mask boards and decrease the process steps. This structure is different from that of Zhang and Yang,[30] whose design

focused on the application of increased emitter coverage caused by deeper microgrooved base electrodes on front surface field (FSF-IBC) solar cells. If the grooves reach several micrometers deep or even more, they may greatly induce gap-induced recombination at the back surface, as reported by Kamioka et al.[31] and Ingenito et al.[32] Such case could be occurred in wet etching and laser technologies for the purpose of etching back the emitter from the region where the BSF will be fabricated. Shallow groove ($\approx 1.0\,\mu m$ deep), however, has the characteristic that the bottom of emitter doping is in the same position as the top of BSF doping through controlling the ablation strength and ablation time with laser. As a result, the undiffused gap and the overlap between emitter doping and BSF doping can both be avoided (i.e., from the direction perpendicular to the back surface). Combining with the FFE layer based on "pumping effect" located at the top of IBC solar cell, the designed bottom shallow groove structure could efficiently reduce the recombination of carriers to increase the short-circuit current density (J_{SC}) and facilitate the preparation of low-cost and high-efficiency IBC solar cells. Figure 1b shows the distribution of the cell efficiency and carrier lifetime (τ_{bulk}) in silicon substrate for the superior IBC solar cells. We can see that the more efficient IBC cells generally have a higher carrier lifetime. For the IBC cells to reach 29.4% limiting efficiency, the carrier lifetime needs to be close to 30 ms. The very high carrier lifetime has been reported by literature for the n-type silicon of lightly doped.[33]

We have simulated the main fabrication of the FFE-IBC solar cell of n-type silicon wafer with a thickness of 100 μm and a resistivity of 4.5 Ω cm. The FFE conducting layer near the front surface of silicon wafer was established by the p-type doping. Al_2O_3, SiN_x, and SiO_x were utilized as passivation layer, antireflection layer, and protection layer of the silicon solar cell for the thickness of 20, 75, and 80 nm, respectively. Air/cell front interface was texturized by smoothed pyramids for the base angle of 54.7° and the height of 2.0 μm, which was related to the adopted wet-alkaline etching process. The minority carrier lifetime τ_{bulk} was set to 10.0 ms, which is the prerequisite for high-efficient solar cells, and the previous best reported values could achieve that high τ_{bulk}.[7] Also, detailed influence of τ_{bulk} on cell performance is shown in Figure S1, Supporting Information. Carrier recombination in the interface between Al_2O_3 and p$^+$ Si was set
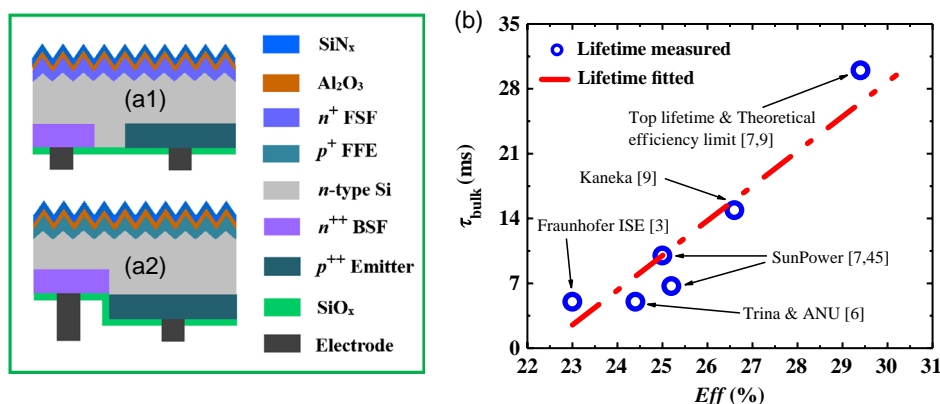
Figure 1. Schematic diagram of a1) reference IBC solar cells and a2) FFE-IBC solar cells with the legends shown on the right. b) A distribution of carrier lifetime and Eff for superior IBC solar cells. The red dotted line corresponds to fitted value for the experimental results.

for the speed of 5 cm s^{-1} on account of the excellent chemical passivation and field effect passivation.[34] Surface recombination speed of 2×10^3 cm s^{-1} was set for undiffused gap, as more power loss can occur with inferior rear surface passivation (see Figure S2, Supporting Information). Default value was adopted here for the carrier recombination of other interfaces. Table SI, Supporting Information, summarized the input parameters of device simulation, and the refractive index (n) and extinction coefficient (k) of the stacks were taken from the literature.[35]

Based on the device construction and software configuration features, a modular two-step 2D numerical simulation was conducted on FDTD solutions (optical simulations) and DEVICE software (electrical simulations), as already successfully adopted by Schnell et al. and Arjmand and Mcguire.[36,37] The first step was to obtain the 2D map of the light absorption and optical generation rate inside the considered device based on 2D Maxwell's equations. The standard reference spectrum AM1.5G at 1 sun irradiance (1000 W m^{-2}) was introduced as the incident light source. Vertical interfaces to the left hand and to the right hand of the simulated domain had been modeled as perfectly reflecting layers to prevent the escaping of light from lateral surfaces and to ensure the periodicity of the symmetry element. The 2D map of the photogenerated electron–hole pairs within the silicon substrate extracted from the optical simulation was then directly deployed into DEVICE software based on drift-diffusion models for exact electrical characteristic calculations. Our modeling approach required a more extended simulation domain for the optical simulation and a tetragonal mesh with fine mesh size

of 0.1 μm in the front-textured morphology and the rear flat groove structure for electrical simulations.

To account for resistive effects of rear side metallic grid (fingers and busbars) from real 3D device to the simulated 2D device, we assumed that current only flows though metallic contacts and that these are equipotential regions. Moreover, a particular calibration of physical models implemented in the numerical Lumerical solutions' simulator had been performed according to sets of the state-of-the-art parameters,[38] as shown in Table SII, Supporting Information. According to these, more reasonable values were used to calibrate the doping-dependent trap-assisted SRH bulk and surface recombination models related to defects in the silicon substrate and at passivated interfaces.

3. Photon Absorption and Electrical Characteristics with FFE Layer

It has been proved in experiment that Al$_2$O$_3$ has superior passivation effect on boron-doped p$^+$ FFE.[18,20,34] We have shown the results in **Figure 2**a. Among the three deposition methods of reactive sputtering, plasma-enhanced chemical vapor deposition (PECVD), and spatial atomic layer deposition (ALD), the third method can make the surface recombination rate S_{eff} drop to about 10 cm s^{-1}. Based on this, the J_{SC} is simulated with various S_{eff} for the two passivating interfaces of Al$_2$O$_3$/n-Si and Al$_2$O$_3$/p$^+$ FFE as shown in Figure 2b. We can see that the Al$_2$O$_3$/p$^+$ FFE interface has better passivation for the whole range. Afterward, we varied the FFE doping concentration in
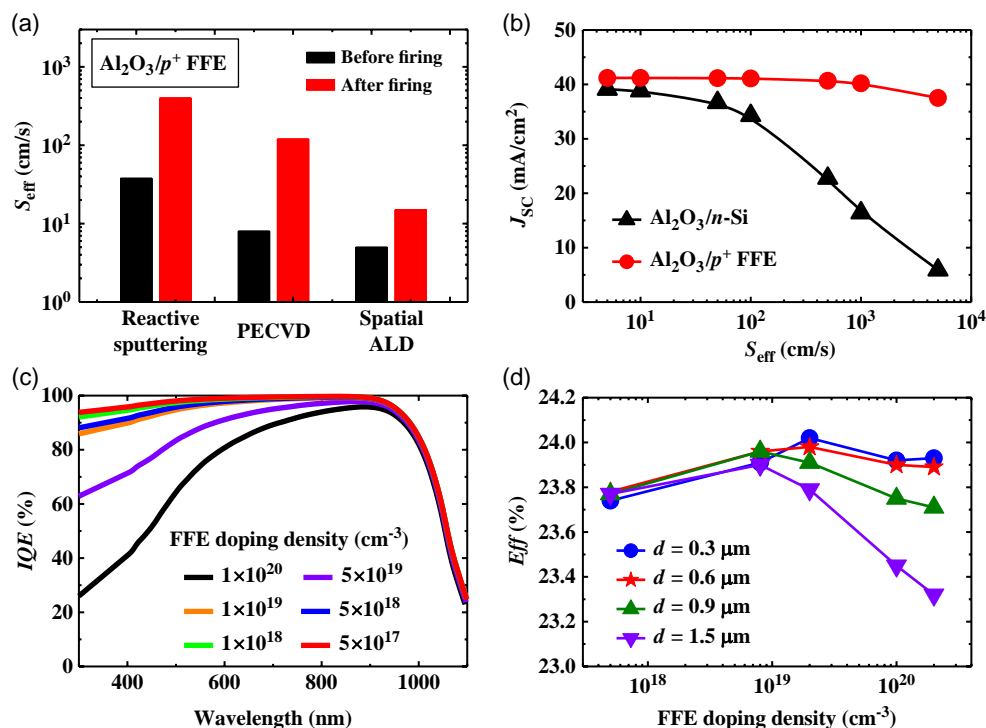
Figure 2. a) Comparison of carrier recombination rate S_{eff} on p$^+$ Si surface coated with Al$_2$O$_3$ formed by three deposited methods. b) Simulated J_{SC} versus different S_{eff} for the interface of Al$_2$O$_3$/n Si and Al$_2$O$_3$/p$^+$ Si. c) IQE of IBC solar cells versus different FFE doping densities in the wavelength of 300–1100 nm. d) Eff of IBC solar cells as a function of different FFE doping densities for various junction depths.

the range of 5×10^{17}–2×10^{20} cm^{-3} and the simulated temperature is always 300 K for room-temperature working solar cells. Figure 2c,d shows the internal quantum efficiency (IQE) and Eff for different FFE doping densities; the multifarious junction depth d is also shown in Figure 2d. We can find that the IQE decreases rapidly in the scope of the medium-short wavelength (300–800 nm) with the increase of FFE doping densities from 5×10^{17} to 1×10^{20} cm^{-3}. This demonstrates that the low-doped FFE can improve the utilization rate of silicon absorption layer on photons of sunlight. However, sheet resistance R_S becomes larger with the decrease in FFE doping concentrations (i.e., from 30.5 Ω □$^{-1}$ with density of 1×10^{20} cm^{-3} to 945.3 Ω □$^{-1}$ with density of 5×10^{17} cm^{-3}), leading to a weaker lateral voltage drop in lower FFE doping density. The reduction of average FFE voltage stem from a different built-in voltage between FFE and base, which depends on FFE or base doping. Hence, high-performance FFE-IBC solar cells could be obtained through optimizing the doping concentration for the FFE layer (Figure 2d), and the first-rank order of magnitude of FFE doping is in the value of about 1–2×10^{19} cm^{-3}.

Furthermore, as shown in Figure 2d, the FFE-IBC solar cell performance is enhanced for smaller doping depth with doping density exceeding 1×10^{19} cm^{-3}, whereas the cell property is not affected by doping depth with lower concentration doping. The enhancement of Eff is profited from the FFE-IBC solar cells fabricated on the emitter with a higher active boron surface concentration and shallower junction depth (called front surface float emitter). We know that high sheet resistance is in favor of the short-wavelength spectral response in solar cells, leading to the promotion of J_{SC}.[39] Nevertheless, excessively low junction depth will not be considered in real solar cells without practical significance. Based on the aforementioned discussion, the FFE doping junction with depth of 0.6 μm with Gaussian distribution function is selected for the extensive calculations, as shown in Figure 2c.

4. Advanced Carrier Collection with Shallow Grooves

For the back side of the FFE-IBC solar cells, **Figure 3**a shows that the Eff is monotonically decreasing with the increase in gap

width, keeping constant the pitch of 1200 μm and 1/2 width ratio of BSF to emitter in the simulation. We know that the variation of resistivity trade-off in the rear region from longer gap could degrade the value of FF of the solar cells.[25] In addition, due to the lack of effective field effect passivation (i.e., preventing the high density carrier from reaching the noncollection interface), undiffused gap would usually result in heavily carrier recombination.[28] In the investigation performed by Reichel et al.,[29] it has been shown that even if the surface passivation is excellent (i.e., the surface recombination rate near the gap is close to 0 cm s^{-1}), the local IQE in the undiffused gap and BSF region on the rear side of IBC solar cells is lower than that in the emitter region for a higher base doping concentration of 1×10^{16} cm^{-3}, leading to a corresponding loss in the J_{SC} of around 2 mA cm^{-2}. Notice that just the recombination rate at the gap is changing. Figure 3b shows that the second-diode recombination current J_0 of rear p–n junction is enlarged with ever-increasing junction densities per centimeter (the higher the junction density, the lower the cell pitch). The value of J_0 is larger than the dark saturation current (generally less than 1 nA cm^{-2}), proving the existence of surface p–n junction recombination. The J_0 increases from 9.5 to 22.0 nA cm^{-2} versus junction densities increase from 5 to 40 cm^{-1} for the S_{gap} of 50 cm s^{-1}, indicating that the pitch cannot be too small. Many previous theoretical studies have shown that the cell efficiency increases with the decrease in pitch because the p–n junction on the surface is not considered.[25,40]

Shallow groove structure is expected to overcome these shortcomings. The recombination rate at the gap here was set to be larger than other interface due to the inferior passivation. Figure 3c shows the change of the cell performance with the depth of shallow groove for different junction densities. Due to the emitter doping depth of 1 μm, the highest cell efficiency is appeared for the groove depth of about 1.0 μm for maximized carrier collection efficiency. Herein, the surface p–n junction could be formed for the overlap of close range doping between emitter and BSF when the groove depth is less than 1.0 μm, and the deeper groove of larger than 1.0 μm would easily give rise to undiffused gap, which both cause lower carrier collection. The improvements of cell efficiency are even more pronounced with higher junction density. The Eff would be increased by about 1.8% and 4.7% relatively with the groove depth changing
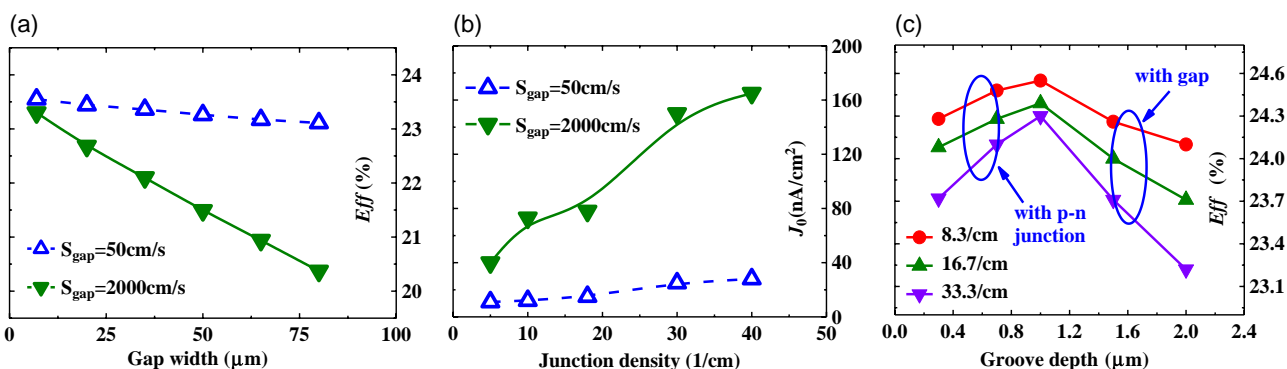
Figure 3. Advantages of shallow grooves for silicon FFE-IBC solar cells. a) Eff of FFE-IBC solar cells with gap versus gap width, b) second-diode current J_0 near the back surface of FFE-IBC solar cells with surface p–n junction versus junction densities, and c) Eff of FFE-IBC solar cells with shallow groove versus groove depth.

1.0 μm for the junction density of 8.3 and 33.3 cm^{-1}, respectively. The corresponding electric field distributions have been shown in Figure S3a2–c2, Supporting Information.

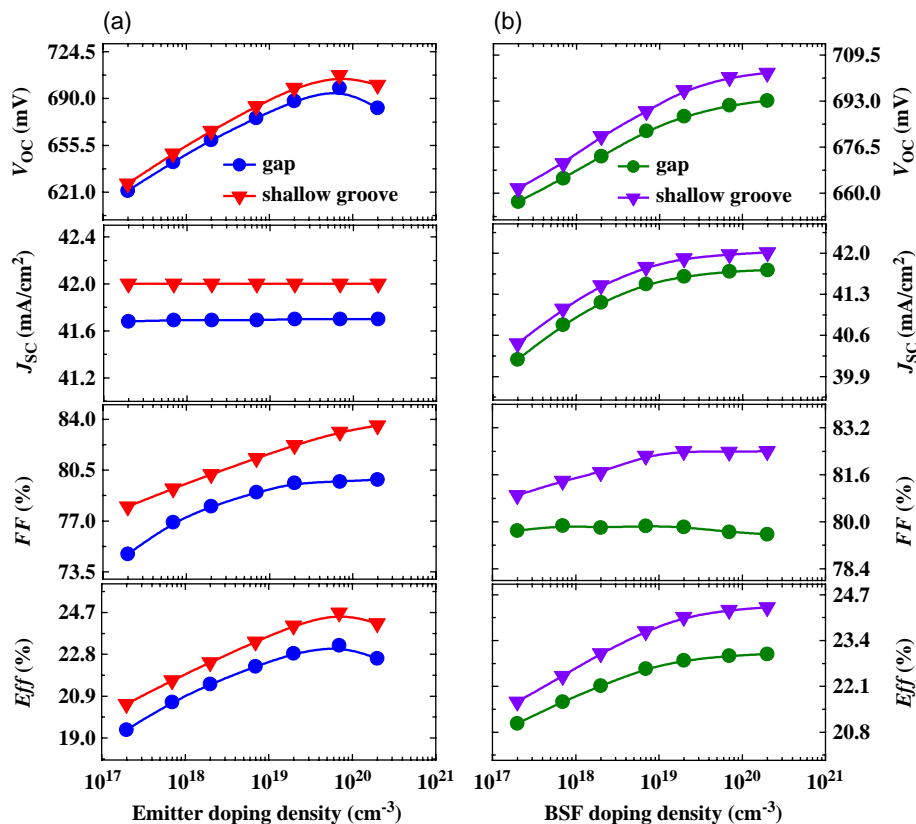## 5. Effect of Shallow Grooves on FFE-IBC Solar Cell Performance

We used the analysis method of a minimum of the total recombination current density under illumination for short-circuit condition to analyze the effect of emitter and BSF doping concentration on cell efficiency. **Figure 4**a,b shows, respectively, the influence of emitter and BSF doping concentrations at both sides of shallow grooves on electrical property of the solar cells. Reference groups are FFE-IBC solar cells with the structure of shallow grooves replaced by gaps. It is clear that both emitter and BSF doping could improve FFE-IBC solar cell performance with shallow grooves relative to that of solar cells with gaps. Figure 4a shows that the V_{OC}, FF, and Eff all have different degrees of improvement with emitter doping less than 8×10^{19} cm^{-3} on both solar cells, and more improvement would be expected for solar cells with the shallow groove structure. One can consider that the apparent change trend of V_{OC} stems from the total saturation current density (i.e., surface, SRH, Auger, and contact recombination current) in dark conditions, and the FF increases by reason of a reduction of the emitter sheet resistance. On the other hand, the V_{OC},

and Eff are descending as the emitter doping concentration is larger than 8×10^{20} cm^{-3} because the enhanced Auger recombination has played a leading role due to the increased boron concentration. In contrast, the J_{SC} remains the same trend due to the fact that the nearby carriers are not affected by "electrical shading." The Eff of FFE-IBC solar cells with shallow grooves can finally increase from 23.2% to 24.7% for the emitter doping density of 8×10^{19} cm^{-3}, which increases by 6.5% relatively compared with the conventional FFE-IBC solar cells.

It is shown in Figure 4b that the V_{OC}, J_{SC}, and Eff all monotonously increase with the BSF doping densities. This is different from the case of the emitter doping in Figure 4a that has originated from the enhancement of high–low junction built-in potential with higher doping, leading to a reduced bulk recombination current. The trend of FF of solar cells with shallow groove, increasing first and then maintaining stability, stem from the reduction of the BSF sheet resistance compared with changeless FF of solar cells with gap. Overall, the Eff can still increase from 23.0% to 24.4% for the BSF doping density of 2×10^{20} cm^{-3}, which increases by 6.1% relatively compared with the conventional FFE-IBC solar cells.
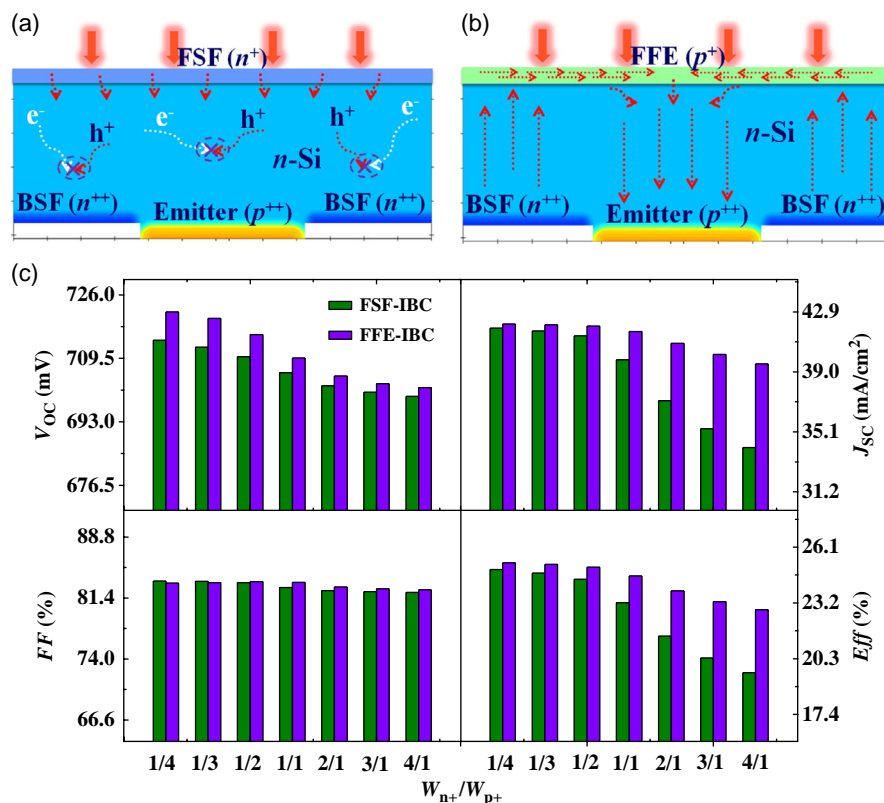
6. Advantage of the FFE-IBC Solar Cells

Figure 5a,b shows the carrier transport and recombination loss schematic diagram of the FSF-IBC and FFE-IBC solar cells with

Figure 4. Effect of shallow grooves on silicon FFE-IBC solar cell performance. Electrical parameters (V_{OC}, J_{SC}, FF, and Eff) for FFE-IBC solar cells with shallow grooves against the reference group with gap under different a) emitter doping densities and b) BSF doping densities.

ADVANCED
SCIENCE NEWS
www.advancedsciencenews.com

physica
pss status
solidi a
www.pss-a.com

Figure 5. Advantage of the silicon FFE-IBC solar cells. Carrier loss schematic diagram of a) the FSF-IBC solar cells and b) the FFE-IBC solar cells with both shallow grooves. c) Electrical parameters (V_{OC}, J_{SC}, FF, and Eff) of FFE-IBC solar cells with shallow grooves versus the ratio of BSF doping width (W_{n+}) to emitter doping width (W_{p+}) compared with those of FSF-IBC solar cells.

both shallow grooves, respectively. The FFE layer could pump minority carriers above the BSF region and then quickly reinject them into the base and transport to emitter region based on the lateral voltage difference inside FFE layer (Figure 5b).[16,37] Therefore, the recombination loss caused by electrical shading and trap-assisted SRH (see Figure 5a) could be reduced to a minimum. Figure 5c shows the optimized performance (V_{OC}, J_{SC}, FF, and Eff) of FFE-IBC solar cells, together with the FSF-IBC solar cells for comparison. The horizontal coordinates are the width ratio of BSF region to emitter region (namely W_{n+}/W_{p+}). We know that the variation trend of V_{OC} is determined by the ratio of the photogenerated current to the reverse saturation current (I_L/I_0).[38] The increased proportion of BSF region in fixed pitch could degrade the I_L/I_0, leading to a descending V_{OC}. It is also clearly shown that the J_{SC} in both the FFE-IBC and FSF-IBC solar cells decreases with the increase in the ratio of W_{n+}/W_{p+}, and the latter decreases drastically. The degradation of J_{SC} is due to the higher "electrical shading" loss caused by wider BSF region in both IBC solar cells for the fixed pitch of 1200 μm. Therefore, the "pumping effect" arising from the FFE layer weaken the carrier recombination loss strength, leading to a slow J_{SC} degradation. Nevertheless, the value of FF is related to the power loss of solar cell series resistance.[39] The series resistance in the calculation models here is very small, which have subtle influence on the variation tendency of FF. As a result, Eff of FFE-IBC solar cells and FSF-IBC solar cells decreases from 25.3% and 24.9% of 1/4 W_{n+}/W_{p+}, respectively, to 22.9% and 19.6% of 4/1 W_{n+}/W_{p+}. The former Eff decreases by 9.5% relatively, compared with the latter of 21.3%, clearly demonstrating that the high-efficiency FFE-IBC solar cells can improve, significantly, the tolerability for the variation of W_{n+}/W_{p+} in IBC solar cells. The simulation result was consistent with that of Dong et al.[41]

The advantage of FFE-IBC solar cells over FSF-IBC solar cells enables minority carrier transport over distances that are larger compared with the typical BSF or emitter width, even though the almost identical trends in cell performance curves can be observed versus front surface recombination in Figure S4, Supporting Information. The width of BSF region and emitter region could be made for the same (namely 1/1 for W_{n+}/W_{p+}) in FFE-IBC solar cells with only a slight sacrifice of photocurrent density and Eff. The conductive FFE layer enables equally sized interdigitated doping patterns of positive and negative polarities on the rear side, with similar cell pitch and efficiency compared with FSF-IBC solar cells. Such a unit cell does not account for important geometric features, such as busbars and pads, edges or interruptions in metallization fingers for IBC construction, which can lead to more freedom in the

interconnection layout and increase the tolerances for the module fabrication due to the allowable lower resolution processing (e.g., standard screen printing).
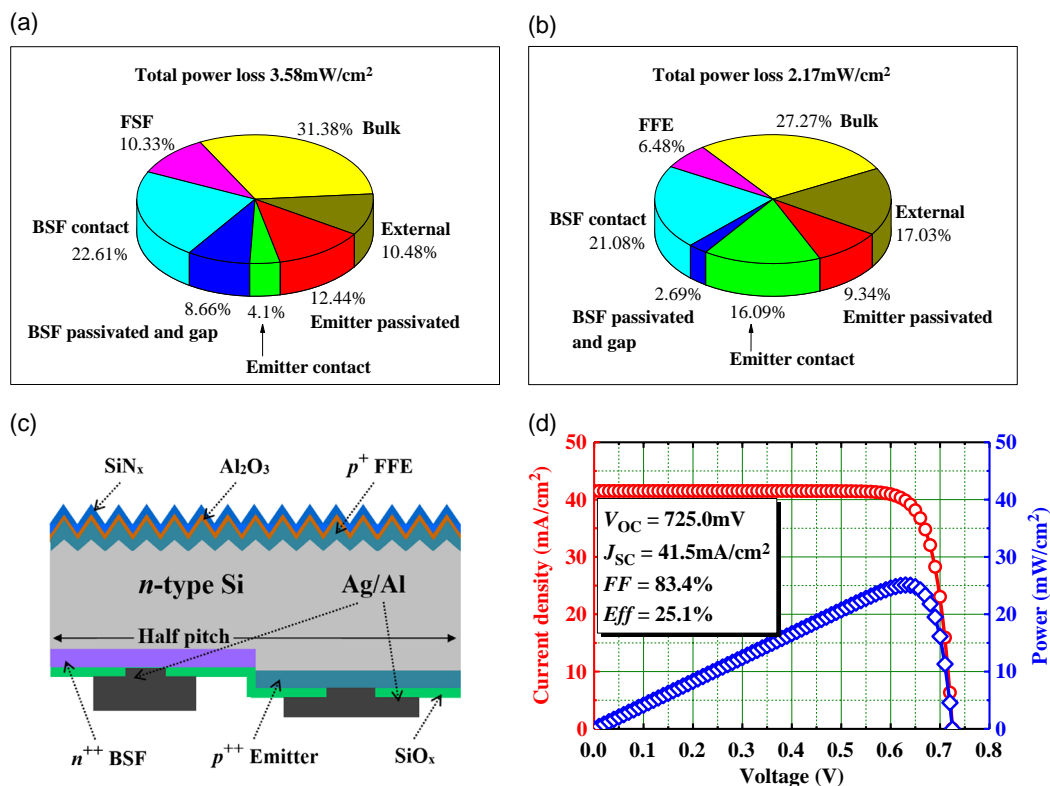
7. Performance of the FFE-IBC Solar Cells

The front surface recombination rate in the interface of Al_2O_3/p^+ FFE was set to $5\,cm\,s^{-1}$, which is smaller than that of Al_2O_3/n^+ FSF of $100\,cm\,s^{-1}$ due to the superior passivation. More detailed parameters setting is seen in Table SIII, Supporting Information. **Figure 6**a,b shows the total power losses calculated of 3.58 and $2.17\,mW\,cm^{-2}$ for FSF-IBC solar cells with gap and FFE-IBC solar cells with shallow groove, respectively. It is found that defect-related bulk, emitter, and BSF losses dominate losses in both solar cells. The front side, rear BSF passivated, and gap losses ($\approx$10%) are relatively smaller in FFE-IBC cells than that of FSF-IBC cells ($\approx$20%). This mainly attributes to the superior passivation of Al_2O_3 to p^+ silicon and the minimization from the negative impact of gap. Noted that the emitter losses account for about the same proportion as BSF losses due to the 1/1 for W_{n+}/W_{p+} (the schematic diagram of silicon FFE-IBC solar cells is shown in Figure 6c. Figure 6d shows the current–voltage ($I–V$) and power–voltage ($P–V$) characteristics of the optimized FFE-IBC solar cells with shallow grooves for the maximum

V_{OC} of $725.0\,mV$, J_{SC} of $41.5\,mA\,cm^{-2}$, FF of 83.4%, and Eff of 25.1% (see in Table SIV, Supporting Information, the comparison).

8. Conclusions

In summary, we have shown theoretically the high efficiency of 25.1% silicon FFE-IBC solar cells with improved crystalline silicon quality, front surface passivation, and novel shallow groove structure. Minority carrier lifetime and resistivity of silicon substrate have been studied and optimized. Al_2O_3/p^+ FFE interface can bring excellent passivation effect. The effect of FFE conductive layer on optical and electrical properties of IBC solar cells has been evaluated by changing the FFE doping concentration and junction depth. With the optimized FFE layer, we have demonstrated that the shallow groove can effectively enhance the carrier collection through minimizing the negative impact of undiffused gap or surface p–n junction. Furthermore, the novel silicon FFE-IBC solar cells can enable minority carrier transport over distances that are larger compared with the typical BSF or emitter width. The width of BSF region and emitter region could be made for the same in the silicon FFE-IBC solar cells with only a slight sacrifice of photocurrent and Eff, leading to more freedom in the interconnection layout of busbars and pads, edges, and metallization fingers. The improvement of the cell fabrication tolerance can make the silicon IBC photovoltaic system a cost-effective energy solution.

Figure 6. Area-weighted distribution of the total power losses for a) the FSF-IBC solar cells with gap and b) the FFE-IBC solar cells with shallow groove. Noted that the BSF region and emitter region were made for the same width in both solar cells, where we showed c) the schematic diagram of FFE-IBC solar cells. d) $I–V$ and $P–V$ curves for the optimized silicon FFE-IBC solar cells.

Conflict of Interest

The authors declare no conflict of interest.

[1] R. J. Schwartz, M. D. Lammert, in *IEEE Int. Electron Devices*, IEEE, Washington, DC **1975**, 350.

[2] M. D. Lammert, R. J. Schwartz, *IEEE Trans. Electron Devices* **1977**, *24*, 337.

[3] C. Reichel, F. Granek, M. Hermle, S. W. Glunz, *Prog. Photovoltaics: Res. Appl.* **2013**, *21*, 1963.

[4] R. Peibst, N. P. Harder, A. Merkle, T. Neubert, S. Kirstein, J. Schmidt, F. Dross, P. Basore, R. Brendel, in *Proc. 28th EU PVSEC, Paris*, WIP - Renewable Energies, Munich, Germany **2013**, p. 971.

[5] B. J. O'Sullivan, M. Debucquoy, S. Singh, A. U. De Castro, M. R. Payo, N. E. Posthuma, I. Gordon, J. Szlufcik, J. Poortmans, in *Proc. 28th EU PVSEC, Paris*, WIP - Renewable Energies, Munich, Germany **2013**, p. 956.

[6] E. Franklin, K. Fong, K. McIntosh, A. Fell, A. Blakers, T. Kho, D. Walter, D. Wang, N. Zin, M. Stocks, E. C. Wang, N. Grant, Y. Wan, Y. Yang, X. Zhang, Z. Feng, P. J. Verlinden, *Prog. Photovoltaics: Res. Appl.* **2016**, *24*, 411.

[7] D. D. Smith, P. Cousins, S. Westerberg, R. D. Jesus-Tabajonda, G. Aniero, Y. C. Shen, *IEEE J. Photovoltaics* **2014**, *4*, 1465.

[8] https://www.trinasolar.com/us/resources/newsroom/trina-solar-announces-new-efficiency-record-2504-large-area-ibc-mono-crystalline (accessed: February 2018).

[9] K. Masuko, M. Shigematsu, T. Hashiguchi, D. Fujishima, M. Kai, N. Yoshimura, T. Yamaguchi, Y. Ichihashi, T. Mishima, N. Matsubara, T. Yamanishi, T. Takahama, M. Taguchi, E. Maruyama, S. Okamoto, *IEEE J. Photovoltaics* **2014**, *4*, 1433.

[10] K. Yoshikawa, H. Kawasaki, W. Yoshida, T. Irie, K. Konishi, K. Nakano, T. Uto, D. Adachi, M. Kanematsu, H. Uzu, *Nat. Energy* **2017**, *2*, 17032.

[11] M. A. Green, Y. Hishikawa, W. Warta, E. D. Dunlop, D. H. Levi, J. Hohl-Ebinger, A. W. Y. Ho-Baillie, *Prog. Photovoltaics: Res. Appl.* **2017**, *25*, 668.

[12] G. L. Lu, J. Q. Wang, Z. Y. Qian, W. Z. Shen, *Prog. Photovoltaics: Res. Appl.* **2017**, *25*, 441.

[13] M. Hermle, F. Granek, O. Schultz-Wittmann, S. W. Glunz, in *Proc. 33rd IEEE PVSC*, IEEE, Piscataway, NJ **2008**, p. 1666.

[14] X. B. Yang, R. Muller, L. J. Xu, Q. Y. Bi, K. Weber, E. Franklin, J. Benick, *IEEE J. Photovoltaics* **2015**, *5*, 87.

[15] I. Cesar, N. Guillevin, A. R. Burgers, A. A. Mewe, M. Koppes, J. Anker, L. J. Geerligs, A. W. Weeber, *Energy Proc.* **2014**, *55*, 633.

[16] A. R. Burgers, N. Guillevin, A. A. Mewe, A. Suvvi, P. Spinelli, A. W. Weeber, I. Cesar, *Energy Proc.* **2015**, *77*, 21.

[17] P. Spinelli, P. Danzl, N. Guillevin, A. Mewe, S. Sawallich, A. Vlooswijk, B. van de Loo, E. Kessels, M. Nagel, I. Cesar, *Energy Proc.* **2016**, *92*, 218.

[18] R. Muller, C. Reichel, J. Schrof, M. Padilla, M. Selinger, I. Geisemeyer, J. Benick, M. Hermle, *Sol. Energy Mater. Sol. Cells* **2015**, *142*, 54.

[19] A. Mewe, P. Spinelli, A. Burgers, G. Janssen, N. Guillevin, B. van de Loo, E. Kessels, A. Ylooswijk, B. Geerligs, I. Cesar, in *Proc. 42nd IEEE PVSC*, IEEE, Piscataway, NJ **2015**, pp. 1–6.

[20] R. Muller, C. Reichel, J. Benick, M. Hermle, *Energy Proc.* **2014**, *55*, 265.

[21] R. Muller, J. Schrof, C. Reichel, J. Benick, M. Hermle, *Appl. Phys. Lett.* **2014**, *105*, 103503.

[22] F. Granek, M. Hermle, S. W. Glunz, *Phys. Status Solidi RRL* **2008**, *2*, 151.

[23] V. D. Mihailetchi, H. F. Chu, G. Galbiati, C. Comparroto, A. Halm, R. Kopecek, *Energy Proc.* **2015**, *77*, 534.

[24] T. Tachibana, K. Tanahashi, T. Mochizuki, K. Shirasawa, H. Takato, *Jpn. J. Appl. Phys.* **2018**, *57*, 040315.

[25] P. Procel, M. Zanuccoli, V. Maccaronio, F. Crupi, G. Cocorullo, P. Magnone, C. Fiegna, *J. Comput. Electron.* **2016**, *15*, 260.

[26] T. Rahman, A. To, M. E. Pollard, N. E. Grant, J. Colwell, D. N. R. Payne, J. D. Murphy, D. M. Bagnall, B. M. Hoex, S. A. Boden, *Prog. Photovoltaics: Res. Appl.* **2018**, *26*, 38.

[27] H. Savin, P. Repo, G. von Gastrow, P. Ortega, E. Calle, M. Garin, R. Alcubilla, *Nat. Energy* **2015**, *10*, 624.

[28] P. Spinelli, B. W. H. van de Loo, A. H. G. Vlooswijk, W. M. M. Kessels, I. Cesar, *IEEE J. Photovoltaics* **2017**, *7*, 1176.

[29] C. Reichel, F. Granek, M. Hermle, S. W. Glunz, *J. Appl. Phys.* **2011**, *109*, 024507.

[30] B. Zhang, J. F. Yang, *Jpn. J. Appl. Phys.* **2015**, *54*, 014301.

[31] T. Kamioka, Y. Hayashi, K. Nakamura, Y. Ohshita, *Jpn. J. Appl. Phys.* **2015**, *54*, 08KD07.

[32] A. Ingenito, O. Isabella, M. Zeman, *Sol. Energy Mater. Sol. Cells* **2016**, *157*, 354.

[33] A. Richter, S. W. Glunz, F. Werner, J. Schmidt, A. Cuevas, *Phys. Rev. B* **2012**, *86*, 165202.

[34] G. Dingemans, M. C. M. van de Sanden, W. M. M. Kessels, *Electrochem. Solid-State Lett.* **2010**, *13*, H76.

[35] D. Palik Edward, in *Handbook of Optical Constants of Solids*, Vol. *3*, Academic, New York **1998**, pp. 529–536 and 662–680.

[36] M. Schnell, P. Alonso-Gonzalez, L. Arzubiaga, F. Casanova, L. E. Hueso, A. Chuvilin, R. Hillenbrand, *Nat. Photonics* **2011**, *5*, 283.

[37] A. Arjmand, D. Mcguire, *Opt. Quantum Electron* **2014**, *46*, 1379.

[38] P. Procel, A. Ingenito, R. De Rose, S. Pierro, F. Crupi, M. Lanuzza, G. Cocorullo, O. Isabella, M. Zeman, *Prog. Photovoltaics: Res. Appl.* **2017**, *25*, 452.

[39] A. Cuevas, D. A. Russell, *Prog. Photovoltaics: Res. Appl.* **2000**, *8*, 603.

[40] S. Jeong, M. D. McGehee, Y. Cui, *Nat. Commun.* **2013**, *4*, 2950.

[41] P. Dong, Y. M. Zhang, H. Guo, C. X. Zhang, J. K. Ma, X. Y. Qu, C. F. Zhang, *Energies* **2018**, *11*, 939.